Settling dynamics of asymmetric rigid fibers

E. J. Tozzi,[1,a)] C. T. Scott,[2] D. Vahey,[2] and D. J. Klingenberg[3]
[1]*Department of Chemical Engineering and Materials Science, University of California Davis, Davis, California 95616, USA*
[2]*USDA Forest Products Laboratory, Madison, Wisconsin 53706, USA*
[3]*Department of Chemical Engineering and Rheology Research Center, University of Wisconsin, Madison, Wisconsin 53706, USA*

(Received 13 July 2010; accepted 3 February 2011; published online 9 March 2011)

The three-dimensional motion of asymmetric rigid fibers settling under gravity in a quiescent fluid was experimentally measured using a pair of cameras located on a movable platform. The particle motion typically consisted of an initial transient after which the particle approached a steady rate of rotation about an axis parallel to the acceleration of gravity, with its center of mass following a helical trajectory. Numerical and analytical methods were used to predict translational and angular velocities as well as the evolution of the fiber orientation as a function of time. A comparison of calculated and measured values shows that it is possible to quantitatively predict complex motions of particles that have highly asymmetric shape. The relations between particle shape and settling trajectory have potential applications for hydrodynamic characterization of fiber shapes and fiber separation. © *2011 American Institute of Physics*. [doi:10.1063/1.3562253]

I. INTRODUCTION

Settling of solid particles in a fluid occurs in multiple industrial applications, ranging from solid-liquid mixers[1] to particle separation using hydrocyclones and decanters.[2] While terminal velocities are a common focus of studies, separations based on settling trajectory have been proposed by Kabala[3] for the case of axisymmetric particles. The analysis of complex settling dynamics problems requires reliable prediction methods. Some examples of successful prediction of hydrodynamic properties of a single settling particle in a quiescent fluid exist. For cylinders settling at low Reynolds numbers, Ui *et al.*[4] used a bead-shell method to quantitatively predict experimental drag coefficients. Jung *et al.*[5] analyzed the motion of towed superhelices and found that the experimentally measured ratio of translational and angular velocities can be quantitatively predicted using the method of regularized stokeslets.[6] Asymmetric particles made of three spheres can reorient when settling, depending on the configuration of the spheres.[7] Particles of industrial interest such as fibers can have coupling between rotational and translational motions. Trajectories of such particles can be helical and have been studied theoretically for idealized propeller-like particles[8] and helices.[9] Experimental and modeling studies of the three-dimensional settling of particles of complex shape are lacking. One of the experimental challenges in studying settling of complex-shaped particles is the need for tracking particle orientations and trajectories in three dimensions for sufficiently long times to obtain useful data. Another challenge is to reliably predict the shape-dependent hydrodynamic properties such as drag and translation-rotation coupling tensors.

In this work, we report the measurements of the three-dimensional translational and angular velocities of sedimenting asymmetric rigid fibers at low Reynolds numbers. Experimental results are compared with numerical and analytical predictions that employ the bead-shell method for evaluating the hydrodynamic forces and torques. We demonstrate that both numerical and analytical methods predict quantitatively the translational velocity, angular velocity, and orientation evolution of highly asymmetric particles. These results show that the numerical approach employed here can reliably predict fiber dynamics and suggest that the same approach may be used to test predictions of fiber dynamics that employ more approximate methods.[10,11]

II. METHODS

A. Experiment

The experimental methods are described in detail in Ref. 12. Here, we briefly summarize these methods. Experiments consisted of releasing fibers of known shape at the center of the top surface of a transparent container made of poly(methyl methacrylate) (PMMA), filled with high-viscosity Newtonian silicone oil (density $\rho = 971\ \mathrm{kg/m^3}$, viscosity of $0.55 < \mu < 1.04\ \mathrm{Pa\ s}$). The fiber trajectory was recorded as a series of video frames captured with two cameras and analyzed after the experiment. The fibers had angular shapes illustrated in Fig. 1; projections of fibers employed are shown in Fig. 2. For more details on fiber shapes, see Ref. 13. The fibers were made by cutting and bending silver-coated copper wire of diameter $D = 0.203$ mm. Fiber lengths L ranged between 6.9 and 11.4 mm (fiber aspect ratio of $34.5 < a_r \equiv L/D < 56.1$). The density of the wire was $\rho_S = 8940\ \mathrm{kg/m^3}$. Using a liquid of high viscosity eliminates undesired liquid currents caused by inertial and convection effects, such as those reported by Zahn *et al.*[14] for particles suspended in water. The fiber Reynolds numbers based on the fiber length and diameter were less than 3.8×10^{-2} and 6.9×10^{-4}, respectively.

a)Electronic mail: ejtozzi@ucdavis.edu.

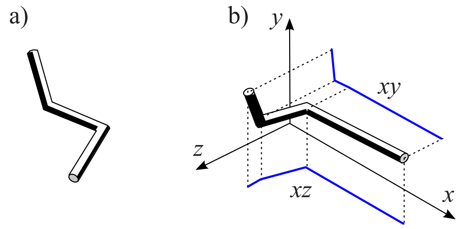

FIG. 1. (Color online) The classes of fiber shapes used are (a) fibers with three noncoplanar segments of approximately the same length and (b) fibers with three noncoplanar segments, one of which is longer than the other two. Projections onto the xy and xz planes are used to show the location of the backbone of the fibers. Pairs of such projections for the fibers used are shown in Fig. 2.

Images of the fibers were acquired with two synchronized Pulnix-TM1325 cameras located, as shown in Fig. 3. More details of the optical system and calculations are given in Appendix A.

In order to keep fibers within the field-of-view at all times with reasonable magnification, the cameras were mounted on a platform that was controllably moved in the vertical direction using a linear motor. The cameras were held at a fixed height as long as a fiber remained inside the field-of-view. When a descending fiber reached the bottom of the field-of-view, the platform was lowered until the fiber appeared at the top of a new field-of-view. This process was repeated until the platform reached the end of its range. The trajectory of descending fibers was imaged along a vertical range of 250 mm. Rulers were mounted behind the cylinder, providing a fixed spatial reference in position calculations. The dual-camera system simultaneously captured pairs of images and their corresponding time stamp. An example of a sequence of captured pairs of images is shown in Fig. 4 (intermediate frames omitted). Orientation was determined using a custom-made computer program described in Ref. 12. The program superimposes an image of a fiber backbone onto the captured images. The operator translates and rotates this "virtual" fiber backbone using the computer keyboard until it is aligned with the actual backbone of the copper fiber in both experimentally acquired images. The position and orientation are then recorded in a file. The process is repeated for all captured frames. The program output is a file with the position and orientation of the fiber corresponding to each image pair.

B. Numerical method

Prediction of fiber motion is based on the analysis of Brenner.[15,16] The hydrodynamic force $\mathbf{F}_H$ exerted on a rigid particle moving with translational velocity $\mathbf{U}$ and rotating with angular velocity $\boldsymbol{\omega}$ in a quiescent fluid is

$$\mathbf{F}_H = -\mathbf{A}\cdot\mathbf{U} - \hat{\mathbf{B}}\cdot\boldsymbol{\omega}, \tag{1}$$

and the hydrodynamic torque is

$$\mathbf{T}_H = -\mathbf{B}\cdot\mathbf{U} - \mathbf{C}\cdot\boldsymbol{\omega}. \tag{2}$$

The tensors $\mathbf{A}$, $\mathbf{B}$, $\hat{\mathbf{B}}$, and $\mathbf{C}$ depend on particle shape and size and are constant in a particle-fixed coordinate system. To compute these tensors, we use the bead-shell method, where particle surfaces are represented as a collection of spheres of radius a.[17–19] The bead-shell model of a fiber is shown alongside photographs of the same in Fig. 5. The number of beads n_{beads} used was in the range of $1329 \le n_{\text{beads}} \le 1972$. Hydrodynamic interactions between the spheres are approximated using the Rotne–Prager–Yamakawa method.[20,21] The sphere centers are displaced by $0.5a$ inside the fiber surface, which was found to provide accurate estimates at reduced computational cost.[12] For the aspect ratios and number of beads used in this work, the offset bead-shell method predicts components of the hydrodynamic tensors of spheroids and cylinders that are within 3% of theoretical values.

For the net gravity force $\mathbf{F}_G$ acting upon a fiber, translational and angular velocities are obtained from

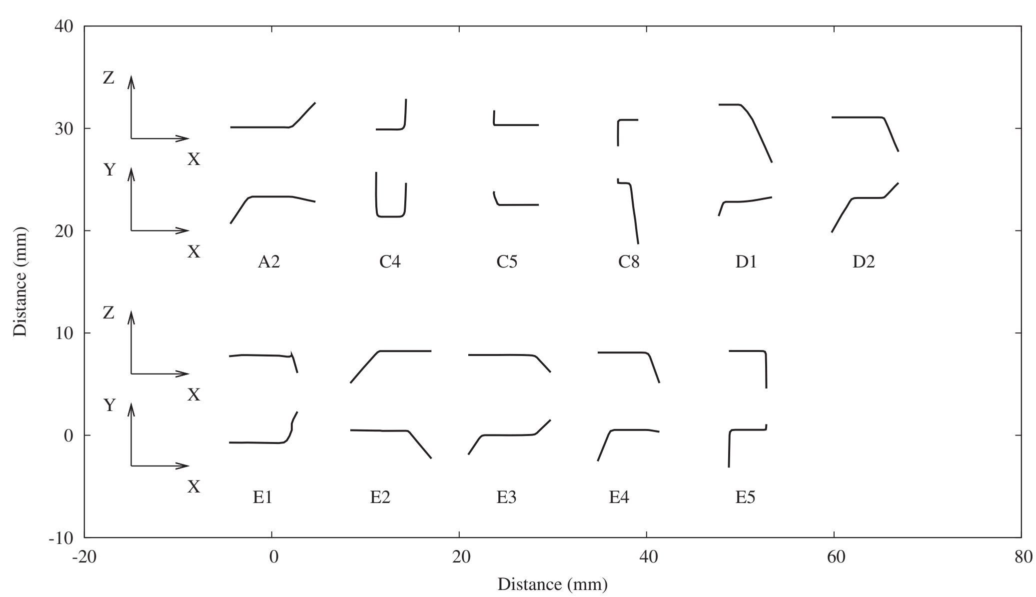

FIG. 2. Projections (xy and xz) of fibers employed. These pictures are drawings created from digitized images of fibers captured with a video camera.

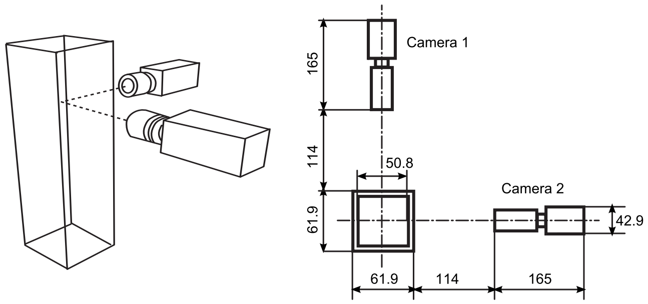

FIG. 3. Diagram of the experimental setup. Dimensions are in mm. Diagram not to scale.

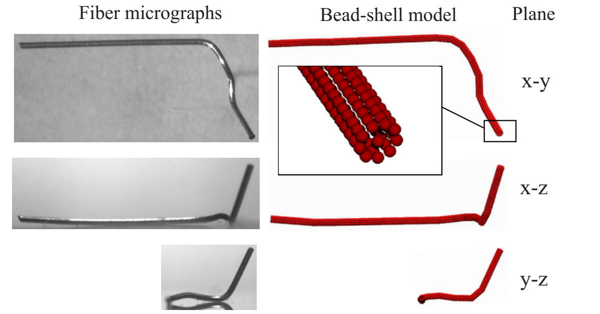

FIG. 5. (Color online) Different views of a fiber and the corresponding views of the bead-shell model of the same fiber.

$$\begin{bmatrix} \mathbf{U} \\ \boldsymbol{\omega} \end{bmatrix} = \begin{bmatrix} \mathbf{A} & \hat{\mathbf{B}} \\ \mathbf{B} & \mathbf{C} \end{bmatrix}^{-1} \cdot \begin{bmatrix} \mathbf{F}_G \\ \mathbf{0} \end{bmatrix} = \begin{bmatrix} \mathbf{a} & \hat{\mathbf{b}} \\ \mathbf{b} & \mathbf{c} \end{bmatrix} \cdot \begin{bmatrix} \mathbf{F}_G \\ \mathbf{0} \end{bmatrix}. \tag{3}$$

Fibers of natural origin can have nonuniform density distribution, which can cause their center of gravity to be located at a different point than their center of buoyancy. In such cases, an additional gravity-buoyancy torque must be added to the model.[22] In this work, we used a material with constant density, and thus the gravity-buoyancy torque is absent.

The fiber translational motion is defined by

$$\dot{\mathbf{r}} = \mathbf{U}, \tag{4}$$

where $\dot{\mathbf{r}}$ is the time derivative of the position vector $\mathbf{r}$.

Particle orientation was represented by Euler parameters,[23,24] which have four components p_0, p_1, p_2, and p_3. The time evolution of the Euler parameters is obtained using

$$\dot{\mathbf{p}} = \tfrac{1}{2}\mathbf{E}^{\dagger} \cdot \boldsymbol{\omega}, \tag{5}$$

where the auxiliary matrix $\mathbf{E}$ is

$$\mathbf{E} = 2\begin{pmatrix} -p_1 & p_0 & -p_3 & p_2 \\ -p_2 & p_3 & p_0 & -p_1 \\ -p_3 & -p_2 & p_1 & p_0 \end{pmatrix}. \tag{6}$$

The body-fixed reference frame is related to the laboratory frame by a rotation matrix $\mathbf{R}$, which is expressed in terms of Euler parameters via

$$\mathbf{R} = 2\begin{pmatrix} p_0^2 + p_1^2 - \frac{1}{2} & p_1p_2 - p_0p_3 & p_1p_3 + p_0p_2 \\ p_1p_2 + p_0p_3 & p_0^2 + p_2^2 - \frac{1}{2} & p_2p_3 - p_0p_1 \\ p_1p_3 - p_0p_2 & p_2p_3 + p_0p_1 & p_0^2 + p_3^2 - \frac{1}{2} \end{pmatrix}. \tag{7}$$

Position and orientation of the fiber as a function of time are obtained by numerical integration of Eqs. (4) and (5) using the Adams–Bashforth predictor-corrector method of order three.[23]

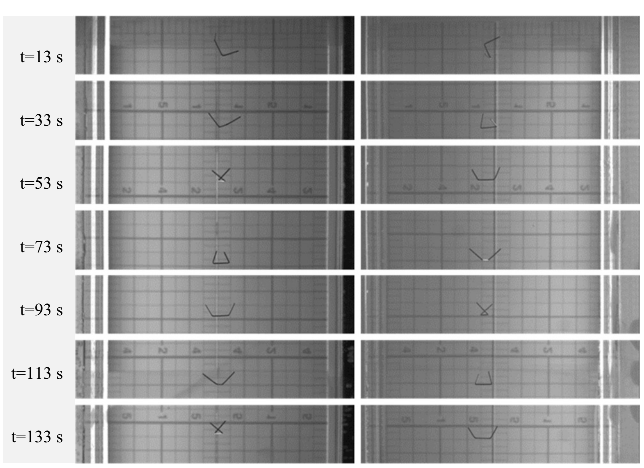

FIG. 4. Examples of captured pairs of images for fiber E5.

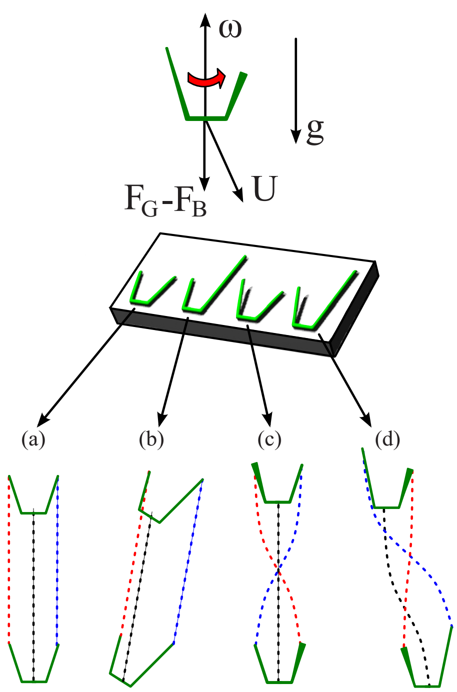

FIG. 6. (Color online) Qualitative motion of fibers having different types of symmetry (see Ref. 8): In all four fibers, the center of buoyancy does not coincide with the center of hydrodynamic resistance, thus the particles have a tendency to reorient to a position where the central segment is below the other two. After this transient reorientation, they can follow various types of asymptotic motion. Particles (a) and (b) have no translation-rotation coupling, and they do not achieve a rotational motion as they fall. In particles (a) and (c), the translational velocity does not have a horizontal component, so they attain a state where their center of mass moves in a vertical fashion. Fiber (b), in contrast, tends to drift sideways with a nonzero horizontal component, falling with a diagonal trajectory. Fiber (d) is like (b), plus it has translation-rotation coupling, and therefore the diagonal fall is compounded with a rotational motion, resulting in a helical path.

TABLE I. Translational vertical velocity (mm/s) of fibers.

Fiber	Experimental (slope)	Numerical (slope)	Numerical (t_{final})	Analytical ($t \to \infty$)
A2	1.89	1.96	2.10	2.10
C4	1.28	1.32	1.33	1.33
C5	1.06	1.03	1.03	1.03
C8	1.11	1.11	1.11	1.11
D1	0.97	1.03	1.03	1.03
D2	1.00	1.03	1.02	1.01
E1	1.00	1.06	1.06	1.06
E2	0.97	1.02	1.02	1.02
E3	0.97	0.97	0.96	0.96
E4	1.04	1.05	1.05	1.05
E5	1.03	1.10	1.10	1.10

TABLE II. Terminal angular velocities (rad/s) of fibers.

Fiber code	Expt.	Analytical	Numerical
A2	−0.024	−0.024	−0.024
C4	0.049	0.050	0.049
C5	−0.024	−0.026	−0.026
C8	−0.021	−0.018	−0.018
D1	0.015	0.013	0.013
D2	0.013	0.014	0.015
E1	−0.010	−0.013	−0.013
E2	−0.009	−0.010	−0.010
E3	0.011	0.009	0.009
E4	0.023	0.025	0.025
E5	0.042	0.041	0.041

C. Analytical method

The asymmetric particles we used in this work belong to the case III.D.a in the classification of Doi and Makino.[8] These particles have hydrodynamic coupling between rotation and translation, and their center of mobility[25] does not coincide with their center of mass. The particles tend to reach a state with a constant angular velocity parallel to the gravity direction. The center of mass tends to follow a helical trajectory[8] with a constant vertical velocity. The angular velocity can be calculated using an eigenvalue analysis if the hydrodynamic resistances are known. From Eq. (3), the angular velocity is

$$\boldsymbol{\omega} = \mathbf{b} \cdot \mathbf{F_G}, \tag{8}$$

where

$$\mathbf{b} = -\mathbf{C}^{-1}\mathbf{B}(\mathbf{A} - \mathbf{B}^{\dagger}\mathbf{C}^{-1}\mathbf{B})^{-1}. \tag{9}$$

As shown by Doi and Makino,[8] for particles with hydrodynamic coupling between rotation and translation, and with a center of mobility that does not coincide with their center of mass, at long times the angular velocity is parallel to the force of gravity, which can be expressed as

$$\boldsymbol{\omega} = \lambda \mathbf{F_G}. \tag{10}$$

Combining Eqs. (8) and (10) gives

$$\mathbf{b} \cdot \mathbf{F_G} = \lambda \cdot \mathbf{F_G}. \tag{11}$$

Equation (11) can be treated as an eigenvalue problem, but it is complicated since $\mathbf{b}$ depends on time. To simplify the analysis, we transform it to the body frame of reference. Tensors $\mathbf{S}'$ in the particle frame of reference are related to tensors $\mathbf{S}$ in the laboratory frame of reference by the relation

$$S_{ij} = R_{ik} S'_{kl} R^{\dagger}_{lj}. \tag{12}$$

Upon transforming frames of reference, we obtain

$$\mathbf{b}' \cdot \mathbf{F_G}' = \lambda \cdot \mathbf{F_G}', \tag{13}$$

where $\mathbf{b}'$ and $\mathbf{F_G}'$ are now time independent and λ need to be solved once for each fiber shape. The parameter λ is the real eigenvalue of the matrix $\mathbf{b}'$. The steady-state angular velocity is subsequently obtained via Eq. (10).

The terminal translational velocity $\mathbf{U}'$ in particle coordinates is

$$\mathbf{U}' = \mathbf{a}' \cdot \mathbf{F_G}', \tag{14}$$

where

$$\mathbf{a}' = (\mathbf{A}' - \mathbf{B}'^{\dagger}\mathbf{C}'^{-1}\mathbf{B}')^{-1}. \tag{15}$$

The translational velocity has a vertical component U_G parallel to gravity of magnitude

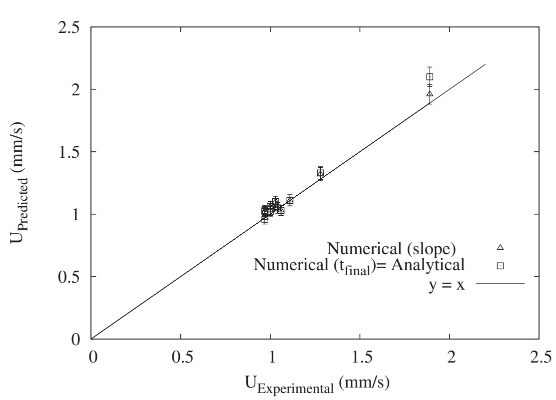

FIG. 7. Comparison of experimental and predicted terminal velocities.

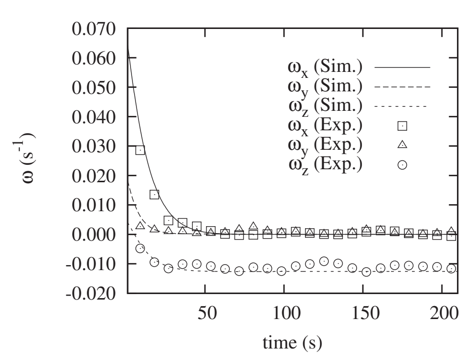

FIG. 8. Experimental and numerically predicted angular velocities as a function of time for fiber E1.

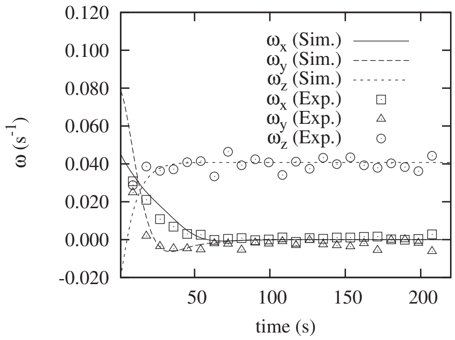

FIG. 9. Experimental and numerically predicted angular velocities as a function of time for fiber E5.

$$U_G = \mathbf{U}' \cdot \mathbf{E}', \tag{16}$$

and a component U_H perpendicular to the gravity direction of magnitude

$$U_H = |\mathbf{U}' \cdot (\mathbf{I} - \mathbf{E}'\mathbf{E}')|, \tag{17}$$

where $\mathbf{E}'$ is the unit vector parallel to gravity.

Therefore, if the hydrodynamic resistances are known, one can predict analytically the vertical and horizontal components of the translational velocity at long times and the angular velocity for an asymmetric particle. The three-dimensional trajectory in this case corresponds to a helix. The horizontal components of the velocity are periodic, which produces a circular motion with a tangential velocity magnitude U_H when the fiber center of mass motion is projected onto a plane normal to the direction of gravity. The radius r_H of the circle and helix is

$$r_H = \frac{U_H}{\omega}. \tag{18}$$

III. RESULTS AND DISCUSSION

During the initial qualitative tests, it was observed that fibers made of three segments settled following roughly four types of motion shown in Fig. 6. We focused the subsequent quantitative study on cases (c) and (d) due to their richer dynamics that includes rotation, and the reduced tendency of these particles to drift toward the container wall.

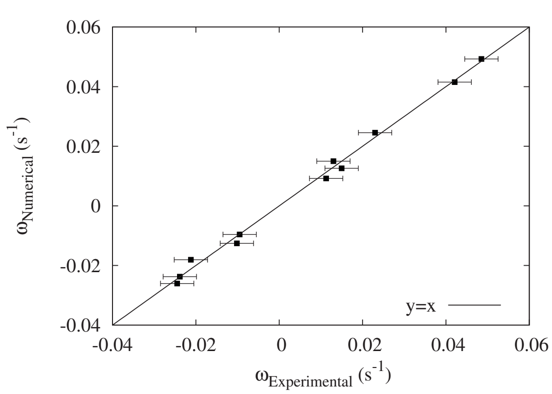

FIG. 10. Correlation between experimental and numerically predicted terminal angular velocities.

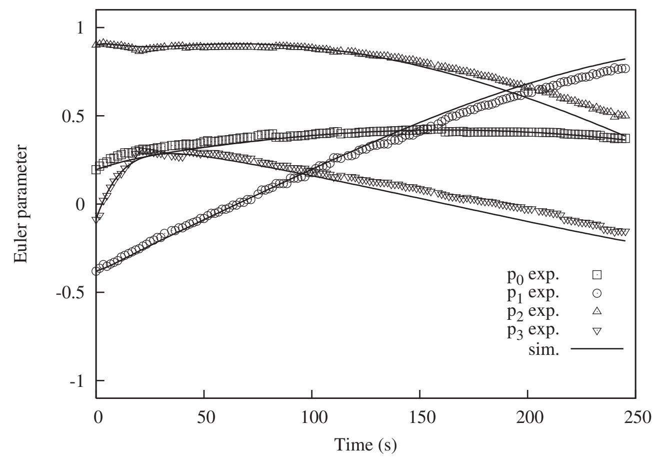

FIG. 11. Experimental and numerically computed Euler parameters as a function of time for fiber E1.

A. Translational vertical velocity

Experimental and predicted translational vertical velocity magnitudes are listed in Table I. The experimental vertical velocity was calculated as the slope of the experimentally measured vertical position as a function of time. The analytical terminal velocity was calculated using the method in Sec. II C. The method in Sec. II B was used to obtain numerically predicted vertical positions as a function of time, from which two types of numerical vertical velocities were calculated: (a) average vertical velocity, calculated as the slope of the vertical positions as a function of time, and (b) instantaneous vertical velocity at the last time point, calculated as the time derivative of the vertical position at the last time point. The numerical instantaneous velocity at the final time coincided with the analytical prediction within the numerical precision, indicating that at the final time, the velocity was indistinguishable from an asymptotic terminal velocity. Experimental and predicted vertical velocities, compared in Fig. 7, are in good agreement, with some differences between instantaneous and average velocities due to the transient time needed to reach the terminal velocity. A noticeable feature in the figure is that several fibers with different shapes have similar

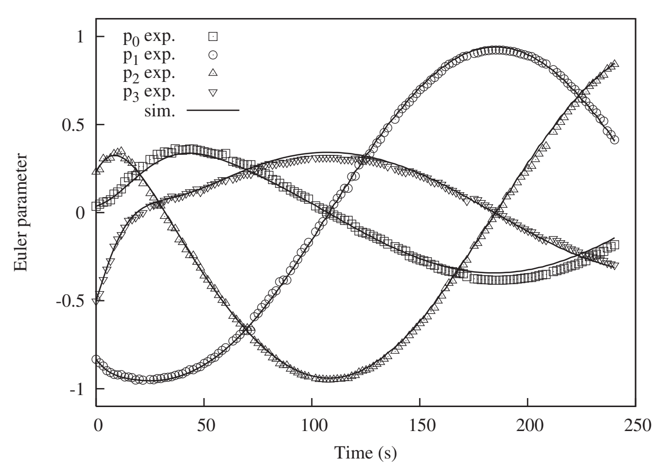

FIG. 12. Experimental and numerically computed Euler parameters as a function of time for fiber E5.

vertical velocities of approximately 1 mm/s. This insensitivity of the vertical velocity to fiber shape is in contrast with the effect of fiber shape on angular velocity, which is discussed below.

Percent differences between experimental and predicted average vertical velocities were defined as

$$\text{Difference\%} = 100\frac{|U_{\text{predicted}} - U_{\text{expt}}|}{U_{\text{expt}}} \tag{19}$$

and ranged from 0.2% to 7.6%. The uncertainty of the predictions (error bars) is dominated by translational elements of the grand matrix calculation,[12] and is estimated to be 4%.

In the results presented above, fibers remained at least 1.17 fiber lengths from the container walls. In preliminary tests performed with fibers descending near the wall (at distances less than a fiber length), the experimentally measured terminal velocity was 10%–15% smaller than the numerically predicted terminal velocity obtained ignoring wall effects.

B. Angular velocity

Experimental and predicted angular velocities are shown in Table II. Experimental angular velocities were calculated from the experimentally measured Euler parameters using[23]

$$\boldsymbol{\omega} = 2\mathbf{E}\cdot\dot{\mathbf{p}}. \tag{20}$$

To obtain time derivatives $\dot{\mathbf{p}}$ of the experimental Euler parameters, the data were smoothed using a regularization method.[26] The time evolution of the x, y, and z components of the angular velocity is plotted for two fibers in Figs. 8 and 9. The x and y components decay to zero rapidly, whereas the z component reaches a steady value (terminal angular velocity). A similar behavior was observed for all fibers. Predicted analytical velocities were obtained directly using the methods described in Secs. II B and II C. The largest uncertainties are due to the experimental measurements, which are about 0.004 s^{-1}. Experimental and predicted angular velocities, compared in Fig. 10, are in agreement within experimental uncertainty. The fibers that had similar vertical velocities close to 1 mm/s had terminal angular velocities that varied widely in magnitude and sign, indicating that angular velocities are more sensitive to fiber shape than the vertical velocity. The time required to reach steady state was estimated from plots of the angular velocity as a function of time, which showed an initial transient, and reached a constant value typically after a period of 20%–30% of the total time of the experiment.

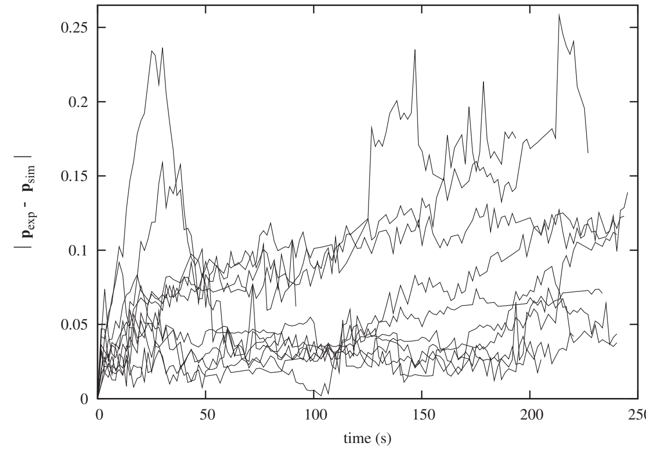

FIG. 13. Time evolution of the magnitude of the difference between experimental and numerical Euler parameters for all fibers studied.

C. Particle orientation

Changes of particle orientation with time are reflected in the time evolution of the Euler parameters. In Figs. 11 and 12, the time evolution of experimental and predicted Euler parameter components for two fibers is presented. Similar agreement was observed for the other fibers. The magnitude of the absolute difference between the experimentally measured and predicted orientation $|\Delta p|$ can be calculated as

$$|\Delta p| = |\mathbf{p}^{\text{expt}} - \mathbf{p}^{\text{sim}}| = \sqrt{(p_0^{\text{expt}} - p_0^{\text{sim}})^2 + (p_1^{\text{expt}} - p_1^{\text{sim}})^2 + (p_2^{\text{expt}} - p_2^{\text{sim}})^2 + (p_3^{\text{expt}} - p_3^{\text{sim}})^2}, \tag{21}$$

where the experimentally measured Euler parameter quaternion is $\mathbf{p}^{\text{expt}}$ and the predicted Euler parameter quaternion is $\mathbf{p}^{\text{sim}}$. A difference of zero would indicate the best possible agreement. The time evolution of $|\Delta p|$ is plotted as a function of time for all fibers in Fig. 13. For most fibers, the values remain below 0.1; the difference in magnitude is less than 0.26 for all the fibers. The time averages $\overline{|\Delta p|}$ for each fiber are listed in Table III.

D. Trajectories

Three-dimensional trajectories of the center of mass of the fibers approached a helix at long times, which is typical for asymmetric particles.[8] The helix radius varied from one fiber to another. An example of a trajectory with a large helix radius is shown in Fig. 14. The three-dimensional trajectories predicted numerically agreed qualitatively and sometimes quantitatively with the experimentally measured trajectories. Differences between predicted and measured trajectories are attributed largely to small discrepancies in measured particle shape, which can have a large influence on the radius of the helical trajectory, especially when the angular velocity is small.[12]

To analyze the behavior of the trajectories at long times, we performed simulations where the total time extends beyond the experimental times. In Figs. 15 and 16, we show

TABLE III. Time-averaged difference between measured and predicted Euler parameters.

Fiber code	$\overline{\|\Delta p\|}$
A2	0.071
C4	0.054
C5	0.111
C8	0.111
D1	0.044
D2	0.044
E1	0.066
E2	0.042
E3	0.097
E4	0.028
E5	0.039

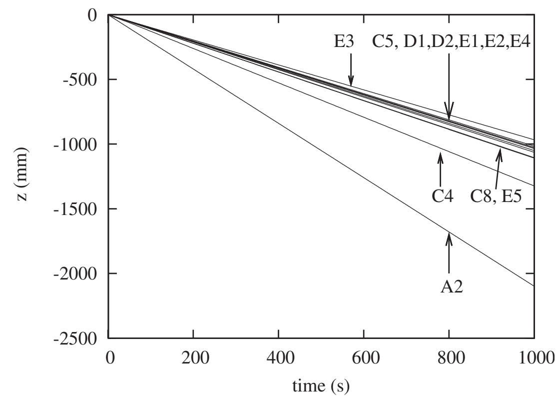

FIG. 15. Vertical coordinate of the fiber center of mass as a function of time obtained through long time-simulations.

that the vertical coordinate of the fiber center of mass decreases linearly as a function of time, and the x-y trajectories of the center of mass approach circular motion. This dynamics corresponds to a helical motion. The helix radius is related to the coupling between rotation and translation. A small coupling will cause slow rotation, and therefore a large radius of the helix. The radii of the helices for the fibers employed here are relatively small, not much larger than the fiber length. It must be noted that the shapes chosen for this study have a strong translation-rotation coupling, and the associated small helix radii are beneficial in avoiding trajectories that would cause fibers to approach or collide with the container walls, thus negating the assumption of negligible wall effects. Fibers with larger helix radius or shapes similar to those in Fig. 6(b) would be of interest in future work to analyze the feasibility of separations by shape.

E. Comparison between bead-shell and free-draining methods

The bead-shell method can be computationally expensive, especially if one must perform computations for fibers that change shape over time (i.e., flexible fibers) or are present in large numbers. In these cases, a simplified hydrodynamic calculation, the so-called free-draining approximation, may be used for convenience. A free-draining method, used previously by Switzer *et al.*,[10] consists of assigning to each cylindrical segment of the fiber the hydrodynamic resistance tensors of a prolate spheroid of aspect ratio 0.7 times the aspect ratio of the segment. We compare the predictions of steady-state translational velocity U and angular velocities ω, obtained using both the bead-shell and the free-draining (FD) method. Fibers with the shape depicted in Fig. 1(a) were used with right angles between segments and overall aspect ratios of $10 \leq a_r \leq 1000$. Table IV shows the ratios between velocities calculated using each method as a function of the fiber aspect ratio. The methods' agreement improves as the aspect ratio is increased.

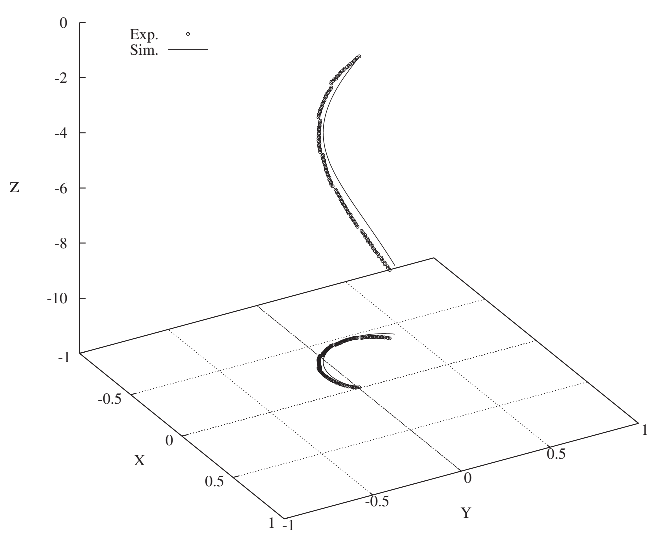

FIG. 14. Three-dimensional center of mass trajectory of fiber E1. The symbols represent experimentally measured positions. The solid curve is the simulated trajectory. Projections of the trajectories onto the bottom plane are also included. Lengths are nondimensionalized by the container's half-width.

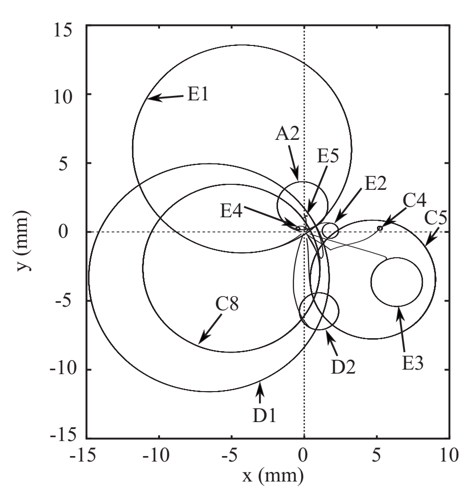

FIG. 16. x-y trajectories of the fiber center of mass obtained through long time-simulations. Fibers are launched at the origin of coordinates.

TABLE IV. Comparison of steady-state vertical and angular velocities obtained using the bead-shell and free-draining methods.

a_r	$U_{\text{bead-shell}}/U_{\text{FD}}$	$\omega_{\text{bead-shell}}/\omega_{\text{FD}}$
10	2.63	7.08
33	1.92	1.50
100	1.64	1.24
200	1.52	1.18
1000	1.41	1.14

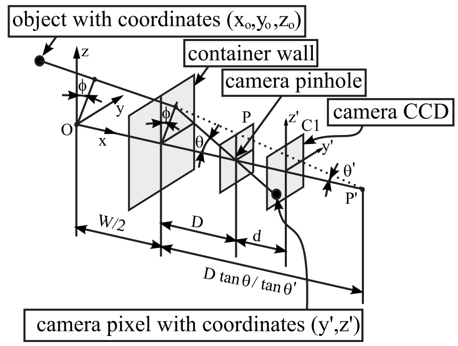

FIG. 17. Path of a light ray in the imaging system.

IV. CONCLUSIONS

To our knowledge, this is the first time predictions based on a bead-shell method are compared with sedimentation experiments using asymmetric particles with translation-rotation coupling. The agreement between measured, numerical, and analytical predictions of fiber motion indicates that settling of single fibers of complex shape can be reliably modeled with the proposed methods. The agreement is not unexpected since Ui *et al.*[4] found an agreement between the measured drag of cylinders and the values predicted using a bead-shell method.

A consequence of the findings is that separation methods based on complex sedimentation trajectories can be designed in future work using the methods described. The particles used in this study had highly three-dimensional and chiral shapes that facilitated the unambiguous experimental measurement of their orientation, but such measurements might be more challenging for other shapes, such as particles that deviate slightly from a symmetric shape (i.e., slightly curved cylinder). For such experimentally "difficult" shapes, the numerical or analytical methods described can still be used to predict settling dynamics. We also observed that particle trajectories have helix radii that depend on particle shape. Such radii can be very different even for particles with similar terminal translational velocities. Therefore, settling experiments provide additional information about the hydrodynamic properties of a complex-shaped fiber in addition to the terminal velocity. The relation between settling dynamics and particle geometry suggests that the angular velocity, trajectory, or radius of the helical trajectory can be used as a tool to characterize fibers, or to detect changes in particle characteristics in an industrial process.

In addition to predicting settling dynamics, the agreement between measured and predicted properties suggests that the bead-shell method can be exploited to predict the dynamics of bodies in other flows. The bead-shell method can in principle be used to examine rigid, nonstraight fiber dynamics in dilute suspension flows. This method can be used to critically evaluate more approximate methods for determining the dynamics of complex-shaped bodies, such as the free-draining approximation employed in the simulation of flexible fibers described elsewhere.[10,11] Here, we showed that for a specific fiber shape, the agreement of the sedimentation dynamics predicted using the bead-shell and free-draining approximations improved as the fiber aspect ratio was increased.

ACKNOWLEDGMENTS

The project was supported in part by the National Research Initiative of the USDA Cooperative State Research, Education and Extension Service, Grant No. 2006-35504-17401.

APPENDIX A: OPTICAL ANALYSIS

The requirement of optical analysis is to transform two-dimensional pixel coordinates from two cameras to three-dimensional (3D) spatial coordinates in the container. The first complication is refraction at the interfaces between the three materials: air, PMMA [with a refractive index $n=1.49$ (Ref. 27)], and silicone oil (United Chemical Technologies, Bristol, PA, USA; $n=1.403$, manufacturer specification). Refraction at the PMMA-oil interface is ignored due to the small value of the wall thickness ($w=5.6$ mm) and the small refractive-index difference between the two materials. Figure 17 shows the path of a light ray from a point at coordinate (x_o, y_o, z_o) in the container to the pixel (y', z') in one of the cameras. The external width of the container is $W=61.9$ mm. A yz coordinate plane is centered in the container. The camera's optical axis is the x axis. Following Sutton,[28] the camera is modeled as a pinhole P and a coupled charge device chip $C1$, located at distances D and $D+d$ from the container, respectively. The camera is pointing toward the origin of coordinates, point O.

The refraction angle at the container wall is described by Snell's law,

$$\theta' = \sin^{-1}[\sin(\theta)/n] \approx \theta/n, \tag{A1}$$

where θ' and θ are angles that the internal and external rays make with the x axis, respectively. The approximation in Eq. (A1) is valid at small values of θ. In this work, the error from using the small-angle approximation is much less than the other errors, such as calibration errors involved in the determination of D and d. At the point of refraction, the ray intersects the container wall at ($x=W/2$, $y=D\tan\theta\sin\phi$, $z=D\tan\theta\cos\phi$). From this point, the ray trajectory inside the container appears to originate from point P'. The equations for the ray in parametric form are, for $-W/2 \le x \le W/2$,

$$y(x) = [D\tan\theta + (W/2)\tan\theta' - x\tan\theta']\sin\phi \tag{A2}$$

and

$$z(x) = [D \tan \theta + (W/2)\tan \theta' - x \tan \theta']\cos \phi. \quad \text{(A3)}$$

A second camera is like the first, except rotated 90° to look at the container from the positive y axis. The camera-based coordinate system is (x_2', z_2'), where the x_2' axis is opposite the external x axis. Ray trajectories are described by equations like Eqs. (A2) and (A3) except for the interchange of x and different values of θ, θ', and ϕ. Subscripts 1 and 2 are introduced to differentiate the two cameras. From Fig. 17, for camera 1,

$$\tan \theta_1 = \sqrt{(y_1'^2 + z_1'^2)}/d, \quad \text{(A4)}$$

$$\cos \phi_1 = - z_1'/\sqrt{(y_1'^2 + z_1'^2)}, \quad \text{(A5)}$$

and

$$\sin \phi_1 = - y_1'/\sqrt{(y_1'^2 + z_1'^2)}. \quad \text{(A6)}$$

Equations for camera 2 are similar except for subscripts and the replacement of y_1' by $-x_2'$. Appropriate substitutions of Eqs. (A1) and (A4)–(A6) into Eqs. (A2) and (A3) for camera 1 lead to

$$y_o = - y_1'\left\{\frac{D}{d} + \left(\frac{W}{2n} - \frac{x_o}{n}\right) \times\left[(y_1'^2 + z_1'^2)\left(1 - \frac{1}{n^2}\right) + d^2\right]^{-1/2}\right\} \quad \text{(A7)}$$

and

$$z_o = - z_1'\left\{\frac{D}{d} + \left(\frac{W}{2n} - \frac{x_o}{n}\right) \times\left[(y_1'^2 + z_1'^2)\left(1 - \frac{1}{n^2}\right) + d^2\right]^{-1/2}\right\}. \quad \text{(A8)}$$

The equations for camera 2 are

$$x_o = x_2'\left\{\frac{D}{d} + \left(\frac{W}{2n} - \frac{y_o}{n}\right)\left[(x_2'^2 + z_2'^2)\left(1 - \frac{1}{n^2}\right) + d^2\right]^{-1/2}\right\} \quad \text{(A9)}$$

and

$$z_o = - z_2'\left\{\frac{D}{d} + \left(\frac{W}{2n} - \frac{y_o}{n}\right) \times\left[(x_2'^2 + z_2'^2)\left(1 - \frac{1}{n^2}\right) + d^2\right]^{-1/2}\right\}. \quad \text{(A10)}$$

Equations (A8) and (A10) overdetermine the variable z_o. With proper alignment, however, the equations will give the same solution for z_o. Equations (A7)–(A10) are solved using an iteration scheme. Initial estimates of x_o, y_o, and z_o are obtained from the approximate form of Eq. (A1) for the small-angle regime. The square-root term in Eqs. (A7)–(A10) can be replaced by $1/d$, and the equations have the solutions

$$x_o = \left(nD + \frac{W}{2}\right)\left[\frac{x_2'(nd + y_1')}{n^2d^2 + x_2'y_1'}\right], \quad \text{(A11)}$$

$$y_o = -\left(nD + \frac{W}{2}\right)\left[\frac{y_1'(nd - x_2')}{n^2d^2 + x_2'y_1'}\right], \quad \text{(A12)}$$

$$z_o = -\left(\frac{z_1'}{nd}\right)\left(nD + \frac{W}{2} - x_o\right), \quad \text{(A13)}$$

or

$$z_o = -\left(\frac{z_2'}{nd}\right)\left(nD + \frac{W}{2} - y_o\right). \quad \text{(A14)}$$

Keep in mind that the primed coordinates in this derivation are based on the camera chip, and they are inverted by the imaging electronics. In our experiments, $D=196.1$ mm and $d=34.5$ mm produce a magnification sufficient to image of 50 mm of the container's width on the 8.8 mm wide camera chip. A point in the central axis of the container ($x_o=0$ and $y_o=0$) is at the bottom of the camera chip's 6.6 mm vertical field-of-view when it is at height $z_0=+20.86$ mm. The height calculated from the small-angle approximation is 20.84 mm. These values ignore refraction at the container's boundary with the silicone oil. The refractive index of the PMMA container walls is 1.45 and the wall thickness is 5.56 mm. Taking refraction at the PMMA-silicone interface into account, the true height of the point becomes 20.85 mm, only 0.01 mm higher than that obtained using the small-angle approximation.

The key to the measurement lies in the accurate determination of the variables D and d for a pinhole camera, given that a conventional camera is used. One way to do this calibration is to mount rulers to the front and back container surfaces. The camera focus is adjusted midway between the optimal focus for each surface. Heights H_1 and H_2 on the rulers expose the same pixel z' on the camera. The ratio of the two heights is the same as the ratio of the two distances, D and $D+w$, where $w \approx W/n$ is the apparent thickness of the container in the presence of refraction. The ratios H_1/D and z'/d are also equivalent. The solutions for the two unknowns are

$$D = \frac{H_1(W/n)}{H_2 - H_1} \quad \text{(A15)}$$

and

$$d = \frac{z'(W/n)}{H_2 - H_1}. \quad \text{(A16)}$$

The error in D and d is dominated by uncertainty in the denominator. In our calculations, $H_1 - H_2$ is 4.2 mm. The error in the individual height determinations (H_1 or H_2) corresponds to about 2.5 camera pixels, or 0.125 mm. The accuracy in the determination of the height difference is therefore about 4% and is a systematic error in the determination of 3D coordinates inside the container.

APPENDIX B: GEOMETRICAL INTERPRETATION OF EULER PARAMETERS

Euler parameters are commonly used in computational studies of rigid body motion, molecular simulations, and computer graphics due to their mathematical properties that facilitate efficient calculation of the time evolution of rigid body orientations.[24] According to Euler's theorem, any orientation of a body can be achieved by a single rotation from a reference orientation about some axis.[23] The axis about which the orientation takes place is defined by a unit vector **u**. The angle χ of rotation is positive for a counterclockwise rotation (right hand side convention). A set of four Euler parameters p_0, p_1, p_2, and p_3 is defined as

$$p_0 \equiv \cos\frac{\chi}{2}, \tag{B1}$$

$$\begin{bmatrix} p_1 \\ p_2 \\ p_3 \end{bmatrix} \equiv \mathbf{u}\sin\frac{\chi}{2}. \tag{B2}$$

Using orientational equations of motion in terms of Euler parameters prevents the occurrence of singularities that cause difficulties for other forms of orientation representations such as Euler angles.[24] In our simulation method, we use Eq. (5) to compute the evolution of the Euler parameters and Eq. (7) to obtain the orientation matrix **R** from the Euler parameters. The matrix **R** is used to convert vectors and tensors from a body-fixed frame of reference to a laboratory-fixed frame of reference and vice versa.

[1] S. V. Jadhav and V. G. Pangarkar, "Particle-liquid mass transfer in mechanically agitated contactors," Ind. Eng. Chem. Res. **30**, 2496 (1991).
[2] S. I. Green and B. Wong, "Hydrodynamics of individual pulp fibres," Tappi J. **4**, 3 (2005).
[3] Z. J. Kabala, "Maximum inclination path for laminar settling of axisymmetric particles in viscous fluids," J. Environ. Eng. **125**, 97 (1999).
[4] T. J. Ui, R. G. Hussey, and R. P. Roger, "Stokes drag on a cylinder in axial motion," Phys. Fluids **27**, 787 (1984).
[5] S. Jung, K. Mareck, L. Fauci, and M. J. Shelley, "Rotational dynamics of a superhelix in a Stokes fluid," Phys. Fluids **19**, 103105 (2007).
[6] R. Cortez, L. Fauci, and A. Medovikov, "The method of regularized Stokeslets in three dimensions: Analysis, validation and application to helical swimming," Phys. Fluids **17**, 031504 (2005).
[7] M. L. Ekiel-Jeżewska and E. Wajnryb, "Hydrodynamic orienting of asymmetric microobjects under gravity," J. Phys.: Condens. Matter **21**, 204102 (2009).
[8] M. Doi and M. Makino, "Sedimentation of particles of general shape," Phys. Fluids **17**, 043601 (2005).
[9] Y. J. Kim and W. J. Rae, "Stokes-flow sedimentation of a slender-filament helical-coil," PCH, PhysicoChem. Hydrodyn. **11**, 295 (1989).
[10] L. Switzer and D. J. Klingenberg, "Rheology of sheared flexible fiber suspensions via fiber-level simulations," J. Rheol. **47**, 759 (2003).
[11] L. H. Switzer and D. J. Klingenberg, "Flocculation in simulations of sheared fiber suspensions," Int. J. Multiphase Flow **30**, 67 (2004).
[12] E. Tozzi, "Hydrodynamics, rheology and conduction in suspensions of arbitrarily shaped fibers," Ph.D. thesis, University of Wisconsin-Madison, 2008.
[13] See supplementary material at http://dx.doi.org/10.1063/1.3562253 for detailed coordinates of the fibers.
[14] K. Zahn, R. Lenke, and G. Maret, "Friction coefficient of rod-like chains of spheres at very-low Reynolds-numbers: I. Experiment," J. Phys. II **4**, 555 (1994).
[15] H. Brenner, "The Stokes resistance of an arbitrary particle—II. An extension," Chem. Eng. Sci. **19**, 599 (1964).
[16] H. Brenner and M. E. O'Neil, "On the Stokes resistance of multiparticle systems in a linear shear field," Chem. Eng. Sci. **27**, 1421 (1972).
[17] V. A. Bloomfield, W. O. Dalton, and K. E. Van Holde, "Frictional coefficients of multisubunit structures: I. Theory," Biopolymers **5**, 149 (1967).
[18] E. Swanson and D. C. Teller, "The low Reynolds number translational friction of ellipsoids, cylinders, dumbbells, and hollow spherical caps. Numerical testing of the validity of the modified Oseen tensor in computing the friction of objects modeled as beads on a shell," J. Chem. Phys. **68**, 5097 (1978).
[19] B. Carrasco and J. Garcia de la Torre, "Hydrodynamic properties of rigid particles: Comparison of different modeling and computational procedures," Biophys. J. **76**, 3044 (1999).
[20] J. Rotne and S. Prager, "Variational treatment of hydrodynamic interaction in polymers," J. Chem. Phys. **50**, 4831 (1969).
[21] H. Yamakawa, "Transport properties of polymer chains in dilute solution: Hydrodynamic interaction," J. Chem. Phys. **53**, 436 (1970).
[22] J. Happel and H. Brenner, *Low Reynolds Number Hydrodynamics* (Martinus Nijhoff, The Hague, 1983).
[23] E. J. Haug, *Computer Aided Kinematics and Dynamics of Mechanical Systems. Volume 1: Basic Methods* (Allyn and Bacon, Needham Heights, MA, 1989).
[24] M. P. Allen and D. J. Tildesley, *Computer Simulation of Liquids* (Oxford University Press, New York, 1987).
[25] S. Kim and S. J. Karrila, *Microhydrodynamics: Principles and Selected Applications* (Butterworth-Heinemann, Stoneham, MA, 1991).
[26] J. J. Stickel, "Data smoothing and numerical differentiation by a regularization method," Comput. Chem. Eng. **34**, 467 (2010).
[27] R. Budwig, "Refractive-index matching methods for liquid flow investigations," Exp. Fluids **17**, 350 (1994).
[28] M. A. Sutton, S. R. McNeill, J. D. Helm, and Y. J. Chao, "Advances in two-dimensional and three-dimensional computer vision," in *Photo-Mechanics*, Topics in Applied Physics Vol. 77, edited by P. K. Rastogi (Springer, Berlin, Heidelberg, 2000), pp. 323–372.